Postacquisition Suppression of Large-Vessel BOLD Signals in High-Resolution fMRI

Ravi S. Menon[1–3]*

Large-vessel BOLD contamination is a serious impediment to localization of neural activity in high-resolution fMRI studies. A new method is presented which estimates and removes the fraction of BOLD signal that arises from oriented vessels, such as cerebral and pial veins in a voxel, by measuring their influence on the phase angle of the complex valued fMRI time series. A maximum likelihood estimator based on a linear least-squares fit of the BOLD signal phase to the BOLD signal magnitude in a voxel is shown to efficiently suppress the BOLD effect from these larger veins, whose activation is not well colocalized with the neural response. In high-resolution in vivo fMRI data at 4 T, it is estimated that the method is sensitive to the phase changes in the cerebral, larger intracortical, and pial veins. The technique requires no special pulse sequence modifications or acquisition strategies, and is computationally fast and intrinsically robust. Magn Reson Med 47:1–9, 2002. © 2002 Wiley-Liss, Inc.

Key words: BOLD; fMRI; vascular; image processing; neuroimaging

At field strengths of 0.5–7 Tesla (1–5), the intensity changes in MRI observed during functional activation using gradient-echo EPI are dominated by the intravascular BOLD changes in the cortical cerebral veins and larger pial veins (macrovascular BOLD). This increases the effective point spread function of the fMRI technique in high-resolution imaging studies (6,7), since these larger veins can extend from several to tens of millimeters from the site of neuronal activity (8). Even at lower resolutions, larger veins can give rise to uncertainty in localization. For example, the presence of a draining vein in the central sulcus (2,8) makes distinguishing pre- from postcentral gyrus activity in the cortex extremely difficult, with obvious implications for other applications, such as presurgical planning in the motor cortex. While many clever techniques, such as spin-echo EPI, spiral, diffusion-weighted EPI, and perfusion-weighted methodologies, have been proposed to suppress the macrovascular BOLD effect, the use of gradient-echo EPI has been virtually ubiquitous in BOLD applications over the past decade because of its speed, multi-slice capability, ease of acquisition, and robust signal.

The objection to the use of the macrovascular BOLD signal in certain brain mapping applications is based on the inhomogeneous distribution of veins in the brain (Ref. 8 and references therein). Cortical cerebral veins can range from 0.5–2.5 mm in radius and are typically found every 5–30 mm along the cortical surface. Because of the folded nature of the cortex, some of these veins can be found in sulci while yet others cross sulci on their way to venous sinuses. The cerebral veins collect deoxygenated blood received from the pial vein network, a dense, branching collection of 25–250-μm-radius vessels located every 0.2–3 mm along the cortical surface. The smallest pial veins are formed from the right-angle emergence of an intracortical vein (10–60 μm radius) that penetrates the cortex tangential to the surface. These tangential penetrations occur every 0.25–1.5 mm on the cortical surface, and with the associated intracortical arteries form a so-called "vascular unit." Within the context of a few mm³ imaging voxel, the cortical and most pial veins can be considered essentially linear and oriented, while the capillaries (2.5–4 μm radius) and venuoles are more or less randomly oriented. An examination of Duvernoy's work (8) suggests that penetrating intracortical veins of 25–60 μm in radius are the first postcapillary vessels of any length which run with a defined orientation within an imaging voxel, while venuoles and capillaries are effectively randomly oriented when orientations are averaged across the voxel.

For discussion purposes, "macrovascular" will be used to refer to vessels that are greater than the smallest intracortical veins (>25 μm radius), all of which should be oriented. The term "microvasculature" refers to anything smaller than the intracortical veins (<25 μm radius); vessels which are presumably well localized to the columnar organization of the brain and are, to a large extent, randomly oriented in typical voxel sizes used in high-resolution fMRI. In general, the cutoff radius for distinction of micro- vs. macrovascular BOLD will depend on the spatial resolution of the brain function being mapped. For the typical smoothed voxel size of 6 × 6 × 6 mm used in multisubject averages, activation in the venous sinuses is probably the only undesirable quantity. For studies of columnar architecture, the inclusion of the intracortical veins that form vascular units as described above is (theoretically) undesirable, since these units do not correlate one-to-one with functional cortical units. In practice, this imperfect mapping of vascular geometry to functional anatomy may be a subtle obstacle to columnar level mapping.

[1]Laboratory for Functional Magnetic Resonance Research, John P. Robarts Research Institute, London, Ontario, Canada.

[2]Department of Diagnostic Radiology and Nuclear Medicine, University of Western Ontario, London, Ontario, Canada.

[3]Department of Medical Biophysics, University of Western Ontario, London, Ontario, Canada.

*Correspondence to: Dr. Ravi S. Menon, Imaging Research Labs, John P. Robarts Research Institute, P.O. Box 5015, 100 Perth Drive, London, Ontario N6A 5K8, Canada. E-mail: rmenon@irus.rri.ca

With this awareness of the micro- and macrovascular organization, a simple method for suppressing the macrovascular BOLD component is proposed, based on a maximum likelihood estimator derived from a fit of the phase and amplitude time series from a pixel. The method relies on the fact that oriented vessels, which occupy a certain blood volume fraction of a voxel, will produce both magnitude and phase changes in the complex valued MRI signal from the voxel during activation, whereas vessels with random orientation will produce only magnitude changes. It can be demonstrated empirically that the relationship between magnitude changes and phase changes in voxels is linear. One can demonstrate that the method suppresses the BOLD signal from cortical cerebral veins, most pial veins, and larger intracortical veins.

THEORY

Vector Model of the BOLD Signal

Blood vessels have a magnetic susceptibility difference relative to tissue water, $\Delta\chi$, which is sensitive to the fractional oxygen saturation, Y, of hemoglobin. Notably, the frequency pertubation, ω, caused by deoxyhemoglobin containing capillaries and veins can extend beyond the boundary of the vessel (see Eqs. [1] and [2]) (9). Typically, models of the BOLD effect begin with a consideration of the magnetic field or frequency offset inside and outside of a single vessel oriented at some angle with respect to the static magnetic field and occupying some volume fraction of a prototypical imaging voxel (10). The actual concentration of paramagnetic deoxyhemoglobin in the vessel is accounted for via the hematocrit and Y. With reference to Fig. 1, in a single cylindrical vessel at angle θ with respect to the main magnetic field ($B_o = 4$ T), the intravascular ($r < a$) NMR frequency is given by

$$\omega_{iv} = 484.6 \, (1 - Y) \, (3 \cos^2 \theta - 1)/3, \qquad [1]$$

while the extravascular ($r \geq a$) resonant frequency is given by

$$\omega_{ev} = 484.6 \, (1 - Y) \, (a/r)^2 \sin^2 \theta \cos 2 \varphi. \qquad [2]$$

The radius of the cylinder is a, the distance from the central axis of the cylinder to the position of interest along
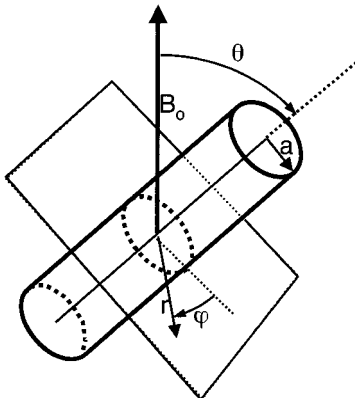

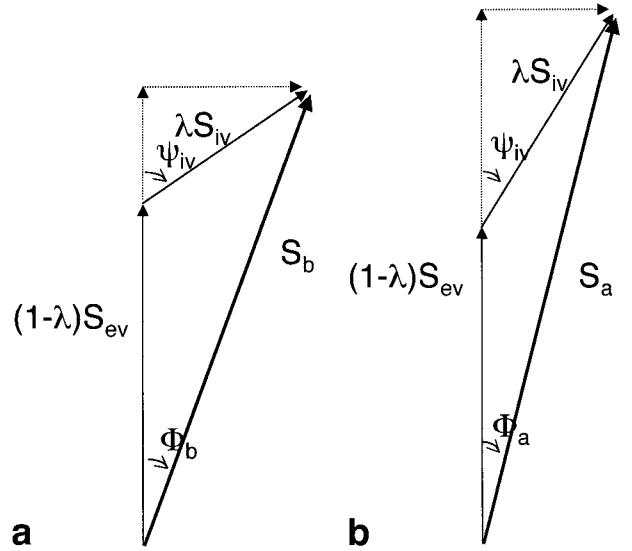FIG. 1. Summary of radius vectors and angles used in Eqs. [1] and [2].

FIG. 2. **a:** Vector model of the BOLD signal S in a voxel during a baseline condition. **b:** Vector model of the BOLD signal S in a voxel during the activated condition. Implicit in the terms S are the T_2 and T_2^* relaxation weightings. The volume fraction of the magnetization in each compartment is explicitly factored in through λ and $1 - \lambda$.

a plane perpendicular to the cylinder axis is r, and the angle between the vector r and the component of B_o projected on this perpendicular plane is φ. The scale factor of 484.6 is derived from a hematocrit (Hct) of 0.4 and a susceptibility difference ($\Delta\chi$) between fully oxygenated and fully deoxygenated red blood cells of 0.18 ppm (11), although a careful recent report measures this as 0.27 ppm (12). Specifically, the value 484.6 is derived from the expression in Eq. [3]:

$$484.6 = 2\pi\gamma\Delta\chi B_0 \, \text{Hct} \qquad [3]$$

where γ is 2.678×10^8 rad T^{-1} s^{-1}, $\Delta\chi$ is 0.18×10^{-6}, and B_o is 4 T.

In addition to the intravoxel dephasing terms that arise from the frequency differences in Eqs. [1] and [2] (2,13), the NMR signal from a voxel in a BOLD fMRI experiment includes T_2 relaxation-modulated contributions from the intra- (S_{iv}) and extravascular (S_{ev}) water magnetization in vessels. Thus, any model that considers the effects of intravoxel dephasing must also include the effects of T_2 relaxation in the two compartments. Qualitatively, T_2 relaxation reduces the expected effect of intravoxel dephasing, because the intravascular signal decays rapidly relative to the extravascular signal on the venous side of the vasculature (essentially disappearing at typical echo times (TEs) at 7 T (5)). Both the intravascular T_2 and the intravoxel dephasing are Y dependent. The major contributors to the BOLD signal that have been discussed are represented in vector form in Fig. 2a, adapted from the work of Hoogenraad et al. (13). Because of the symmetry of the extravascular magnetic field perturbation (cos2 φ term in Eq. [2]), the extravascular spins in a voxel tend to have a near-zero net phase, while the intravascular spins have a coherent phase shift relative to the rotating frame (Eq. [1]

and Ref. 13). This time-dependent intravascular phase term (Ψ_{iv}) will cause a beat between the intravascular NMR signal (S_{iv}) and the extravascular NMR signal (S_{ev}), causing the magnetization in the voxel to vary in amplitude (S) and phase (Φ). Previous reports have considered the MRI signal properties of the intravascular compartment as a significant part of the voxel volume (2,13). One can go beyond this by looking for very subtle effects which cannot be seen in single images, but which can be revealed because of the statistical power realized through the repetitive nature of the fMRI technique.

In typical BOLD experiments, mean relative changes (ΔS) in the magnitude of the voxel magnetization vector (S) are measured during brain activation (S_a) relative to some baseline average (S_b), using a gradient-recalled echo sequence such as EPI ($\Delta S = S_a - S_b$). During the hyperoxic conditions found under increased neural activation, S increases in length because: 1) S_{iv} lengthens as the oxygenation-dependent blood T_2 increases, and 2) Φ changes as the oxygenation-dependent phase difference between the intra- and extravascular proton pools (Ψ_{iv}) changes. The "activated" situation is shown in Fig. 2b. Countering the increase in S is a small decrease in the multiplicative term ($1 - \lambda$) in front of S_{ev} due to a slight increase in the blood volume λ, but the fact that S is observed to increase suggests that the two oxygenation-dependent effects discussed above dominate. The examination of Fig. 2 leads us to the hypothesis that oxygenation-induced changes (ΔS) in S must be related to oxygenation-induced changes ($\Delta\Phi$) in Φ, as *one cannot occur without the other*. As discussed above, changes in Φ are likely to be observable only if vessels giving rise to S_{iv} are not randomly oriented (as a population) within the voxel, and have a sufficient blood volume for the phase change to be detectable above the noise. It is this phase shift Φ that provides the mechanism to separate the macrovasculature BOLD contribution from the microvascular BOLD contribution in a voxel using the complex-valued reconstructed images. While other methods, such as diffusion-weighted acquisitions, conceivably could be used to extract the phase Ψ_{iv} directly, in a conventional EPI sequence the only quantity available is the complex valued NMR signal from the whole voxel ($S \, e^{i\Phi}$).

METHODS

fMRI

The functional imaging experiments utilized in this study were performed using a Varian Unity *INOVA* 4 Tesla whole-body system (Varian NMR Instruments, Palo Alto, CA) equipped with 40 mT/m Siemens Sonata gradients and amplifiers (Siemens, Erlangen, Germany). A variety of motion stimuli were presented in a 50° × 40° visual field to the subjects, via an LCD projector, custom optics, a mirror, and a screen. Data from four subjects were utilized from a study looking at columnar organization in human motion areas MT/MST. The studies were approved by the Ethics Review Board for Human Subjects, of the University of Western Ontario. For the data presented in this work, two protocols are relevant. In the first, a random dot field that appeared to move toward the subject (flow field protocol) and a stationary fixation point were presented in a

block paradigm (24-s baseline, 24-s stimulus) × 4 plus a final 24-s baseline (54 volumes in total). In the second (motion localizer protocol), coherently translating dots in each of eight directions were presented in a block paradigm (96-s baseline, 48-s stimulus) × 6 plus pre- and poststimulus baselines for a total of 216 volumes. A quadrature surface coil with two overlapping 9 × 9 cm elements was used for both RF transmit and receive and was located on the left side of the occipital pole, centered halfway between area MT/MST and V1. Prior to the beginning of the fMRI experiment, T_1-weighted sagittal MR images were collected to prescribe oblique slices in the posterior occipital pole. During the fMRI experiment, T_2^*-weighted MR images at this oblique orientation were collected using a segmented gradient-recalled-echo EPI pulse sequence (7). A four-segment centrically ordered EPI sequence filling a 128 × 128 matrix was used (FOV = 14 × 14 cm). The slice thickness was 2 mm for each of the 11 slices. A TE of 15 ms and a TR of 1 s per segment was used, resulting in an acquisition time of 4 s per volume (1 s × 4 interleaved segments). The flip angle was nominally 45°, roughly the Ernst angle for a TR of 1 s at 4 T. A navigator echo ($k_y = 0$ line was used to make a first-order correction to the data from each segment to compensate for the phase differences that occur between segments due to respiration, etc. For Nyquist ghost removal, a non-phase-encoded full k-space reference for each slice (acquired as the first volume in each experiment) was used to phase-correct the EPI images (14). Unlike typical two-line reference schemes, this approach also effectively reduces off-resonance-induced distortions in EPI images and, in conjunction with our segmented EPI approach, yields fMRI maps that are in excellent registration with the anatomic data (7). Image signal-to-noise ratio (SNR) (signal mean in a 1 × 1 cm region of interest (ROI) in the brain divided by signal mean in a 1 × 1 cm ROI in a corner of the image matrix) varied between 30:1 and 60:1 in the ROIs for this study, and the Nyquist ghost was typically < 2%.

Image Analysis

Brain activation maps were derived from conventional magnitude recontruction, as well as from a micro- and a macrovasculature-sensitive reconstruction, as follows. As a starting point, complex-valued image series of 54 (flow field protocol) or 216 (motion localizer protocol) multi-slice volumes were reconstructed from the phase-reference and navigator-echo-corrected EPI k-space data using a 2DFT with no zero-padding. For each pixel in each slice a phase time series could be derived from the real ($R(i)$) and the imaginary ($I(i)$) components of the pixel using $\Phi(i) = \tan^{-1}(R(i)/I(i))$, where i is the EPI volume index (1–54 or 1–216 here). The phase was unwrapped for every pixel if necessary. Similarly, a time series of the magnitude of the pixel ($S(i) = |R(i) + I(i)| = (R(i)^2 + I(i)^2)^{0.5}$) was also calculated. A minimization of the chi-squared function (15):

$$\chi^2(\Phi, S) = \sum_{i=1}^{N} (S(i) - B - A\Phi(i))^2/((\sigma_S)^2 + (A^2\sigma_\Phi)^2) \quad [4]$$

was performed over the N volumes. The values of the standard deviations (SDs) of $S(i)$ and $\Phi(i)$ were σ_S and σ_Φ, respectively, which were assumed to be normally distributed and the same at every time point. The σ_S and σ_Φ estimates were derived from the SD of the time series by notch filtering $S(i)$ and $\Phi(i)$ at the paradigm frequency and its first four harmonics, and assuming the remaining variation was due to noise. Error estimates for A and B were determined (15). The choice of this polynomial order is further discussed below. The fit parameters were used to produce a maximum likelihood estimator, $S_{est}(i) = A\Phi + B$, of the amount of the changes in $S(i)$ that could be accounted for by changes in $\Phi(i)$ in a least-squares sense. As a final step, $S_{est}(i)$ was subtracted from $S(i)$ to yield the macrovasculature-suppressed BOLD signal, i.e., the microvascular BOLD signal. This procedure was performed for every pixel and for every slice in code written in C, operating on the k-space data. The image volumes derived from the subtraction of $S_{est}(i)$ from $S(i)$ were termed the "microvascular" images, while those made from $S_{est}(i)$ itself were termed "macrovascular" images. The use of $S_{est}(i)$ for calculating the macrovascular images rather than $\Phi(i)$ was predicated by the fact that the phase changes could be of any sign during activation, while the fitted estimator had the same directional changes as conventional BOLD, making comparison of the activation maps more straightforward. Images derived from $S(i)$ were the conventional "magnitude" BOLD images. Each of the microvascular, macrovascular, and magnitude image data sets were analyzed for paradigm-related activation using a t-test between all baseline and activation periods in Stimulate 5.7 (16) at a P value of 0.95. These activation maps were superimposed on the T_1-weighted anatomic images. No minimum threshold was used in the analysis presented below, but a cluster size of 2 was used for the display of the maps. The primary effect of this cluster requirement was to eliminate isolated false-positive pixels that were in the background outside the brain.

RESULTS

First, the validity of using a linear fit of the phase to the magnitude time series was explored. Figure 3 shows the typical relationship of $\Phi(i)$ to $S(i)$ for a voxel from the motion localizer protocol, in which an obvious vessel was present (the dark line in the image) and for a voxel where no visible vein was present (but not implying that vessels larger than venuoles and capillaries were not present). The mean percentage change in BOLD magnitude from this stimulus was 7.5% (corresponding to $\Delta\Phi = 0.085$ radians) for the vein containing voxel and 1.2% (corresponding to $\Delta\Phi = -0.028$ radians) for the other voxel. The slope of $\Phi(i)$ vs $S(i)$ was positive for one voxel and negative for the other. For both the sets of points shown here, the slope of the fit (A from the least-squares minimization) was significantly different from zero, as determined from the error estimates of the fit ($A = 0.88 \pm 0.03$ for pixel with the obvious vein, and $A = -0.43 \pm 0.04$ for the more tissue-like pixel), which means that there was some correlation between $\Phi(i)$ and $S(i)$ in both cases.

In Fig. 4 the effect of a non-zero slope A was explored. To derive the data in these plots, the fractional change
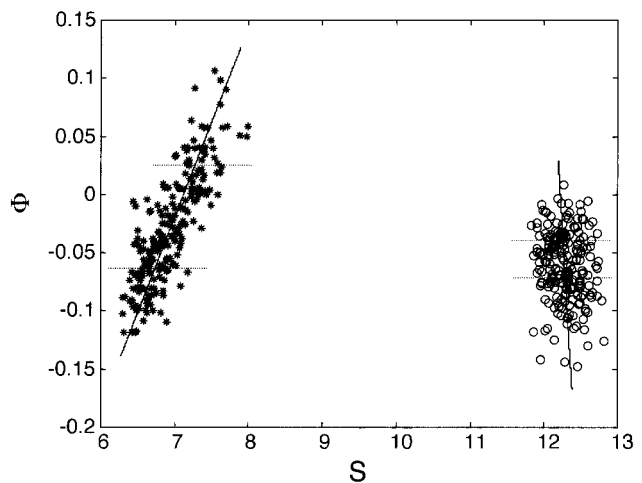

FIG. 3. Phase vs. magnitude signal change for all volumes in a voxel with an obvious vein (*) and a voxel visually devoid of large vessels (○). The lines indicate the least-squares fit of Φ to S over all the 216 volumes. The intersection of the solid lines from the fit with the dashed horizontal lines indicate the baseline and activated means of S and Φ for each voxel, with the baseline having the lower signal intensity.

activation maps was first calculated ($\Delta S/S$) from the magnitude reconstruction for each of the 11 slices at a P value of 0.95, as described earlier using data from the flow field protocol (54 volumes). There were 4364 significant pixels in the 11 activation maps derived from the magnitude data. The mean activation-induced phase change ($\Delta\Phi$) vs. the mean fractional activation-induced magnitude change ($\Delta S/S$) for each of these significantly activated magnitude pixels is plotted on Fig. 4a. The pixel phase changes were expressed relative to the phase of the pixel during the baseline condition ($\Delta\Phi = \Phi - \Phi$). It is clear that increases or decreases of BOLD signal magnitude can give rise to phase changes of either sign, presumably depending on the voxel's vascular orientation with respect to the field. Of the 4364 pixels in Fig. 4a, 2868 pixels had A values that were not statistically significant different from zero, implying no correlation between the phase and magnitude time series or changes. These nonsignificant A pixels are plotted in Fig. 4b.

The high-resolution T_1-weighted anatomic image for a selected slice from the fMRI experiment described in the Methods section is shown in Fig. 5a for one subject. A magnified section of the slice is shown in Fig. 5b, where a draining vein in a sulcus is clearly visible. Identification of this vessel as a vein was made by confirming that its appearance in the high-resolution EPI images was dark (1,2,9). In supporting this assignment (other than the obvious fMRI activation in this vessel), it should be noted that arteries appear bright in the T_1-weighted images due to an in-flow effect, and isoluminant with white matter in the EPI images, since $Y = 1$. To demonstrate the efficacy of the technique, many pixel pairs were selected with the aid of the anatomic and EPI images. One pixel was chosen directly on a visible vein (of varying orientation) and the other was located immediately adjacent to the vein pixel, with the anatomic images ensuring its placement in gray
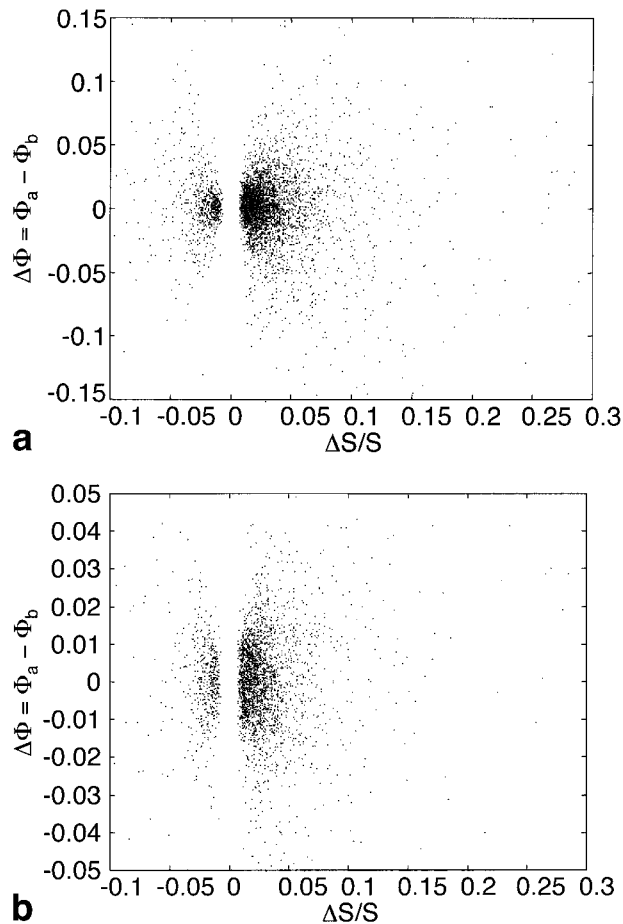
FIG. 4.   **a:** The difference in the voxel phase between the activated and baseline states vs. the fractional signal change in the voxel upon activation for 4364 individual *x,y* pairs. The *x,y* pairs come from 4364 pixels from the 11 slices in one subject who had a significant $\Delta S/S$, at $P = 0.95$. **b:** The difference in the voxel phase between the activated and baseline states vs. the fractional signal change in the voxel upon activation for the subset of 2868 pixels from **a**, in which the least-squares fit of Φ to S did not have a significant slope ($A \sim 0$ in Eq. [3]). These are pixels that show no phase change that correlates with the magnitude changes. Note that the *y* axis differs from that in **a**.

matter (GM). One such pair is shown in Fig. 5c, which will be revisited further below. Time series for another such pair from the motion localizer paradigm (from a different subject and hence not indicated in Fig. 5) are shown in Fig. 6, where the detrended magnitude signal $S(i)$ and the detrended phase signal $\Phi(i)$ are shown for a GM pixel and a vein. Figure 6a shows that in this primarily GM pixel, the phase fluctuations appear somewhat independent of the magnitude fluctuations ($A = -0.94$). However, data from the vein pixel shows obvious phase fluctuations which show some similarity to the magnitude fluctuations, with the paradigm being evident in both S and Φ time series ($A = 6.1$) (Fig. 6b). The A values were derived from a linear least-squares fit, as described earlier between the $S(i)$ and $\Phi(i)$ signals, from which the best fit estimator was derived. This quantity, $S_{est}(i)$, is shown in Fig. 6c and d, where it is quite apparent that very little of the GM magnitude BOLD

signal could be accounted for by Φ fluctuations, while the estimator derived in the case of the vein accounted for a substantial part of the BOLD signal magnitude fluctuations. The estimator was subtracted from the original magnitude signal, as shown in Fig. 6e and f. It is evident that the magnitude signal from the vein is dramatically suppressed, while the GM signal is left virtually untouched. This suppression is reproduced in all visible veins investigated, regardless of orientation.

This same process is demonstrated on a full image basis in Fig. 7, where activation maps made from the magnitude image volumes ($S(i)$), the microvascular image volumes ($S(i)–S_{est}(i)$), and the macrovascular images ($S_{est}(i)$) are shown, overlayed on the anatomic slice shown in Fig. 5. Also shown are the time series from the two pixels shown in Fig. 5c for the flow field protocol. The time series from the vein pixel shows characteristic activation patterns in the magnitude image, as expected. However, in the tissue image, this activity is suppressed and the pixel no longer passes the correlation threshold. The presence of the vessel is clearly indicated in the vein image signal. In the immediately adjacent pixel, located in GM, the magnitude BOLD signal is apparent, and is preserved in the tissue map. In the vein map, however, there is no indication of a venous contribution to the pixel. Note that a cluster size of 2 was set for display purposes and to eliminate pixels outside the head.

DISCUSSION

The simple vector model of BOLD activity in a voxel (Fig. 2) conveys the intuition that changes in S and Φ must be correlated. However, the vector diagram does not address the functional relationship between changes in S and Φ. Knowledge of this relationship is needed for the choice of order in the fitting algorithm used to generate S_{est}. It has been shown empirically in this study, from data such as those in Fig. 3, that regardless of the size of vessels in the voxel and their orientation, a linear fit suffices. The use of a higher-order polynomial improves the chi-square by never more than 11% based on the 35853 activated voxels from the two protocols in the four subjects. Without rigorous simulations, there is no a priori reason to prefer one order of fit vs. the other. Certainly, given the temporal SDs observed, a higher-order model is not warranted. In general, given that the changes in Φ are small ($< |0.2|$ radians), the relationships of the vectors in Fig. 2 can be derived from small-angle approximations, where Φ and $\sin\Phi$ are the same and $\cos\Phi = 1 - \Phi^2$ to within 1%, making a further argument for a linear relationship. Error estimates for A and B were derived from σ_S and σ_Φ. Although σ_S and σ_Φ vary considerably depending on the location of the pixel, for the SNR of the EPI images in these studies the smallest significant group of BOLD changes that could be detected in magnitude activation maps at $P = 0.95$ was on the order of 0.8%, and the smallest group of phase changes that could be detected in phase activation maps at the same P value was on the order of 0.009 radians. In regions of higher vascular pulsatility, these numbers could be twice as high due to a corresponding increase in temporal variance.
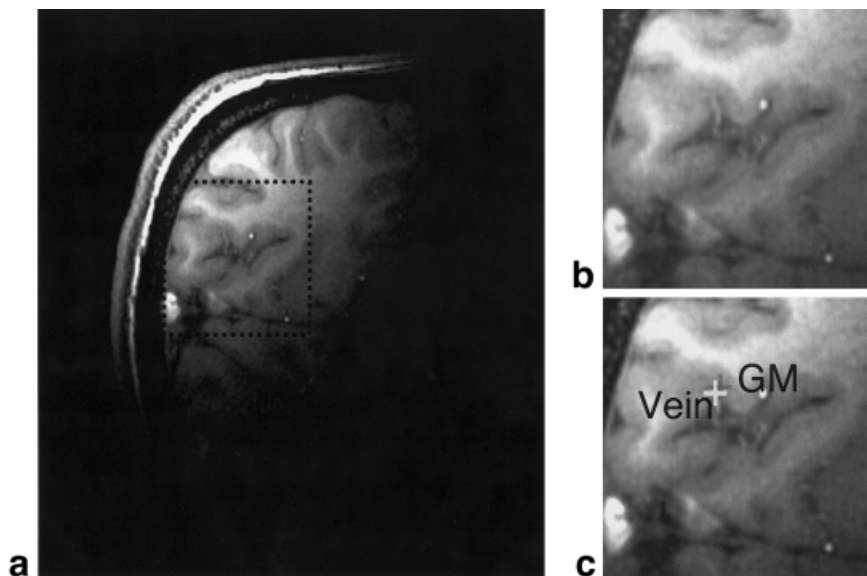
FIG. 5. **a:** High-resolution T_1-weighted scan of slice 8 from subject 3, made with a transmit and receive quadrature surface coil. **b:** A magnification of the box shown in **a**. **c:** Showing the locations from which the GM and vein time series in Fig. 7 were obtained. These two pixels are immediately adjacent in their coordinates.

The other potential confound with my method is that certain voxels containing oriented veins might not be suppressed if the vein were at the magic angle, since A would be zero. Figure 4 suggests that this potential problem is minimal. First, recall that Fig. 4a represents a plot of $\Delta\Phi$ vs. $\Delta S/S$ for pixels with a *statistically significant* $\Delta S/S$. Of the 4864 activated pixels in the functional maps derived from the magnitude image volumes in this protocol, 2868 did not have a value of A that was significantly different from zero. These 2868 pixels are plotted in Fig. 4b. According to my arguments, these pixels could be assigned to tissue or vessels at the magic angle. The mean magnitude change of these pixels was 2.3%, arguing strongly for a tissue assignment based on previous modeling (10,17). However, it was found that 87 of these pixels had magnitude BOLD changes of >10% (chosen on the basis of a secondary peak in the histogram of the fractional magnitude changes), which is potentially indicative of veins in these high-resolution voxels. Closer examination of these 87 pixels showed that all were outside the brain, as were an additional 212 of the group of 2868 pixels with $A \sim 0$ ($\sim$ 27 obvious false-positive pixels per slice). The need to keep track of the obvious false-positive rates in the experiments is the major reason image intensities were not thresholded before performing the t-test, even though this made the computations more time-consuming. Even including these false positives, my observation of a 66% microvascular fraction, i.e., those pixels with $A \sim 0$ (2868/4364) and a $\sim$34% macrovascular fraction, i.e., those pixels with $A \neq 0$ (1496/4364), is in remarkable agreement with studies that have shown that $\sim$40% of the BOLD signal can be suppressed though the use of diffusion-weighted sequences at this field strength (18,19). In the cortex, not a single pixel with a large $\Delta S/S$ (indicative of a vessel) and an A value not significantly different from zero was found.

A small but significant number of negative going pixels were found as well in the activation maps and plots. Some of these were also outside the head, but most were in V1. Their significance is not known, but they may be caused by an inhibition of V1 activity caused by the powerful motion stimuli. Their mean is −1%, and they display phase patterns that are very similar to the BOLD positive response, suggesting similar physical origins.

Having established that a linear fit is an appropriate method to fit Φ to S, and that no obvious vessels are being missed due to orientation effects, I turn to two specific examples of the fitting procedure (Fig. 6) for the motion localizer protocol. The time series are displayed after subtracting out the mean, to enable the reader to see the correlations between the phase and magnitude more clearly. The mean BOLD change in Fig. 6a was 2.6%, while the change in Fig. 6b was 16%. The axes demonstrate that in the GM voxel there was a $\sim$0.03 radian change, while the voxel with the obvious vein had a $\sim$0.15 radian change. The least-squares estimator is shown with the original magnitude time series for each voxel in Fig. 6c and d, wherein it is seen that the voxel with a vein shows a ΔS that can almost completely be accounted for by a scaled representation of $\Delta\Phi$. When the estimator is subtracted, as in Fig. 6e and f, one can see that the activation in the venous voxel no longer appears to be significant.

The fitting procedure relies only on having a reasonable length of time series to work with. Given that most fMRI experiments contain several dozen to hundreds of volumes, this is probably not a significant restriction. Fitting sensitivity can be further enhanced by doing the fit on a band-limited portion of the frequency domain representation of the time series (20). In this way, one can limit the minimization of the chi-square to the paradigm frequency and harmonics. This avenue is being further explored. It has been observed in fits such as these that the method also posseses some motion-suppression properties, particularly at the edges of the brain and around big veins and air-filled sinuses. This may not be too surprising given that motion at these types of edges results in a susceptibility change which affects both S and Φ. An example of a dramatic amplitude correction is shown in the region around volume 55−60 in Fig. 7, where the tissue estimator, S_{est}, shows a corrective increase at these time points that is

FIG. 6. **a:** Phase and magnitude time series from a voxel in subject 1, which was devoid of obvious visible veins and was located in GM. **b:** Phase and magnitude time series from a voxel in subject 1 which had an obvious visible vein and was immediately adjacent to the voxel in Fig. 6a. The time series have been displayed as zero mean to enable visualization of the correlations between them, but the scale for the phase remains correct, being in radians. The time series of S and Φ were fit as described in Methods, and the corresponding maximum likelihood estimator of S is shown as S_{est} in **c** and **d**. The subtraction of this estimator from the original magnitude time series is shown for (**e**) the GM pixel and (**f**) the pixel containing a vein. The vein BOLD signal is effectively suppressed.
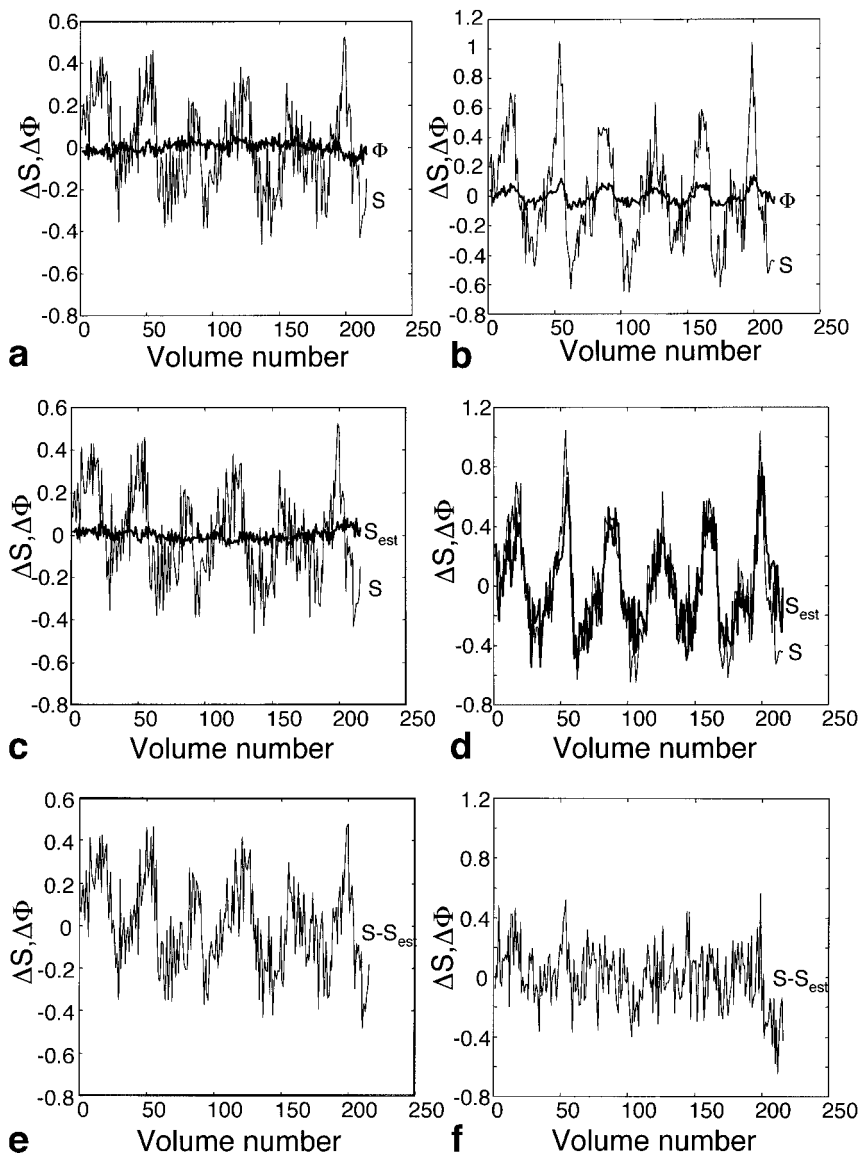
subtracted from the original magnitude signal. This fortuitous property is also being further explored. As far as chest motion is concerned, our navigator echo eliminates the phase fluctuations in the signal due to respiration-induced local field changes, so band-limiting the analysis to avoid B_o-induced phase variations is not critical in this application. If navigator-echo correction is not used when fitting in the temporal domain, the phase changes due to respiration may dominate the chi-square minimization, resulting in poorer fits.

My method has similar properties to the diffusion-weighted suppression of macrovascular BOLD signals (18,19) but does not require the use of a spin-echo EPI sequence with large gradients, with the associated SAR and noise issues. Figure 7 shows that there are many voxels in which both a microvascular component and a macrovascular component can be found. The maximum likelihood estimator removes the macrovascular contribution in the voxel, leaving the microvascular contribution. That is, the method handles partial volume effects cor-

rectly, at least in a least-squares estimator sense. Previously, we and several other groups used an approach in which pixels that exceeded a certain percent change were discarded, purportedly because they were large-vessel in origin. The inadvisability of the threshold approach is further underscored in Fig. 7. Here one can see that the fractional change in the vessel was in fact less than in the adjacent cortex. An amplitude threshold of 3% would have eliminated the tissue signal and kept the vessel. The method does not change the statistics of the activation maps either. The microvascular map in Fig. 7 does not show any additional active areas compared to the conventional magnitude map.

While one cannot quantitatively estimate the vessel size cutoff of my method without BOLD simulations that use realistic vascular geometries, it should be noted that the cutoff is determined by the SNR. My method relies on the correlation of fluctuations in two independent NMR quantities. The minimum justifiable chi-square of the fit is determined by the noise in the signals, and the lower that
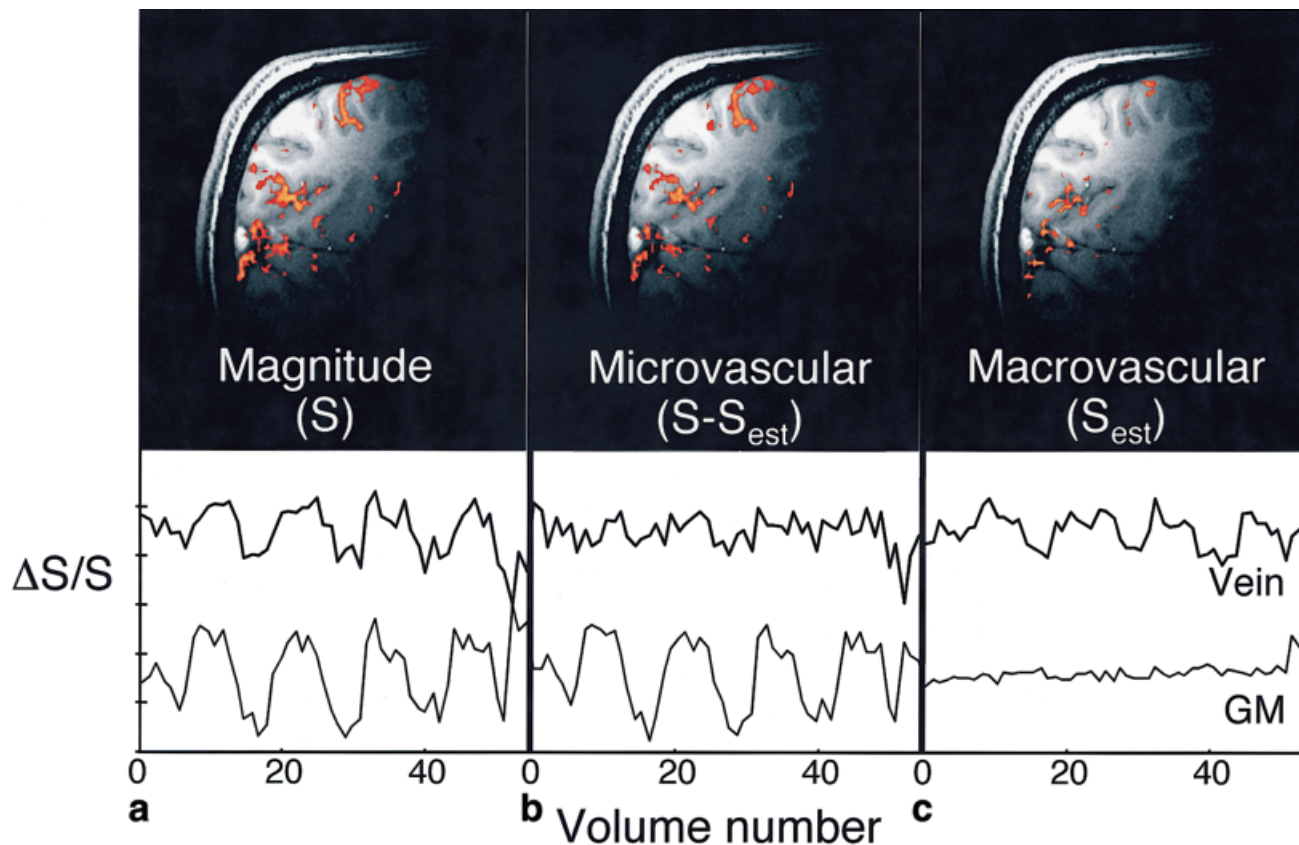
FIG. 7. Activation maps made from slice 8 of subject 3, whose anatomic image is shown in Fig. 5. **a:** The conventional magnitude activation map is shown along with time series from the two voxels marked in Fig. 5c. The vertical tick marks indicate 2% changes. **b:** An activation map made from the microvascular component is shown, and the time series of the vein containing voxel reflects its suppression. **c:** An activation map made from the estimator, which reflects the macrovascular BOLD signal, is shown. Here the vein signal is preserved and no activity is seen in the GM voxel.

noise is, the more sensitive the algorithm. At 4 T, with a TE of 15 ms, one might estimate nominal capillary BOLD changes of 1% (10,17), near the magnitude detection threshold at this resolution. Similarly, a single 50-μm radius vessel parallel to the magnetic field would give rise to a 0.002 radian shift and a magnitude change of 0.5% in a voxel the size (unpublished simulations based on Ref. 17). With minimum detection thresholds of 0.009 radians and 0.8%, we are not quite sensitive to this scenario and one must conclude that BOLD activity from intracortical veins is present in these so-called microvascular activation maps. However, on our scanner, using the same EPI sequence with a 1-cm-thick slice on an oil-filled phantom and an SNR of 1000, the single-pixel temporal SD is about 0.1% and the SD of the phase is better than 0.001 radians over 1000 images. Thus, the human experiments described here are not limited by theoretical considerations, but rather by finite SNR. High-resolution studies done on animals at much higher field strengths will certainly benefit from this method.

CONCLUSION

A method to estimate and remove the fraction of BOLD signal that arises from oriented vessels in a voxel by ob-

serving their influence on the phase angle of the complex valued fMRI time series is presented. It is shown that an estimator based on a linear least-squares fit of the BOLD signal phase to the BOLD signal amplitude can be used to correctly suppress the BOLD effect from larger vessels. While the potential to lose suppression for vessels at the magic angle exists, in practice it is observed that this is not significant. With infinite SNR, the method could suppress BOLD contributions at the level of very small tangential intracortical veins, but with the data shown here, one can estimate that the method is sensitive to the phase changes in the larger intracortical and pial veins, and of course, the larger cerebral veins. The method has several advantages over diffusion-based approaches. It is quieter, since no diffusion-sensitizing gradients are needed. It is less SAR-intensive, since no 180° pulses are needed. The number of slices per unit time is triple that of a spin-echo sequence, since the optimum TE for a spin-echo sequence is roughly triple that for a gradient echo. Finally, diffusion methods are sensitive to motion, while this least-squares approach has the ability to suppress motion-induced changes in the BOLD signal by virtue of the phase changes they produce.

This technique requires no special pulse sequence or acquisition strategies, and is computationally fast and intrinsically robust. It can be applied restrospectively to

archived data, if the original raw *k*-space data have been stored.

REFERENCES

1. Menon RS, Ogawa S, Tank DW, Ugurbil K. 4 Tesla gradient recalled echo characteristics of photic stimulation-induced signal changes in the human primary visual cortex. Magn Reson Med 1993;30:380–386.
2. Lai S, Hopkins AL, Haacke EM, Li D, Wasserman BA, Buckley P, Friedman L, Meltzer H, Hedera P, Friedland R. Identification of vascular structures as a major source of signal contrast in high resolution 2D and 3D functional activation imaging of the motor cortex at 1.5T: preliminary results. Magn Reson Med 1993;30:387–392.
3. Segebarth C, Belle V, Delon C, Massarelli R, Decety J, Le Bas JF, Decorps M, Benabid AL. Functional MRI of the human brain: predominance of signal from extracerebral veins. Neuroreport 1994;5:813–816.
4. Gati JS, Menon RS, Ugurbil K, Rutt BK. Experimental determination of the BOLD field strength dependence in vessels and tissue. Magn Reson Med 1997;38:296–302.
5. Yacoub E, Shmuel A, Pfeuffer J, van de Moortele P-F, Adriany G, Andersen P, Vaughn JT, Merkle H, Ugurbil K, Hu X. Imaging brain function in humans at 7 Tesla. Magn Reson Med 2001;45:588–594.
6. Engel SA, Glover GH, Wandell BA. Retinotopic organization in human visual cortex and the spatial precision of functional MRI. Cereb Cortex 1997;7:181–192.
7. Menon RS, Goodyear BG. Submillimeter functional localization in human striate cortex using BOLD contrast at 4 Tesla: implications for the vascular point-spread function. Magn Reson Med 1999;41:230–235.
8. Duvernoy HM. The human brain: surface, blood supply, and three-dimensional sectional anatomy, 2nd ed. New York: Springer-Verlag; 1999. 491 p.
9. Ogawa S, Lee T, Barrere B. The sensitivity of magnetic resonance image signals of a rat brain to changes in the cerebral venous blood oxygenation. Magn Reson Med 1993;29:205–210.
10. Ogawa S, Menon RS, Tank DW, Kim S-G, Merkle H, Elleman J, Ugurbil K. Functional brain mapping by blood oxygenation level-dependent contrast magnetic resonance imaging. A comparison of signal characteristics with a biophysical model. Biophys J 1993;64:803–812.
11. Weisskoff RM, Kiihne S. MRI susceptometry: image-based measurement of absolute susceptibility of MR contrast agent and human blood. Magn Reson Med 1992;24:375–383.
12. Spees WM, Yablonskiy DA, Oswood MC, Ackerman JJH. Water proton MR properties of human blood at 1.5 Tesla: magnetic susceptibility, T_1, T_2,T_2*, and non-Lorentzian signal behavior. Magn Reson Med 2001;45:533–542.
13. Hoogenraad FG, Reichenbach JR, Haacke EM, Lai S, Kuppusamy K, Sprenger M. In vivo measurement of changes in venous blood-oxygenation with high resolution functional MRI at 0.95 Tesla by measuring changes in susceptibility and velocity. Magn Reson Med 1998;39:97–107.
14. Bruder H, Fischer H, Reinfelder HE, Schmitt F. Image reconstruction for echo planar imaging with nonequidistant k-space sampling. Magn Reson Med 1992;23:311–323.
15. Press WH, Teukolsky SA, Vetterling WT, Flannery BP. Numerical receipes in C, the art of scientific computing, 2nd ed. New York: Cambridge University Press; 1992. 994 p.
16. Strupp SP. Stimulate: a GUI based fMRI analysis software package. NeuroImage 1996;3;S607.
17. Bandettini PA, Wong EC. Effects of biophysical and physiologic parameters on brain activation-induced R2* and R2 changes: simulations using a deterministic diffusion model. Int J Imaging Syst Tech 1995;6:133–152.
18. Menon RS, Hu X, Adriany G, Andersen P, Ogawa S, Ugurbil K. Comparison of spin-echo EPI, asymmetric spin-echo EPI and conventional EPI applied to functional neuroimaging. The effect of flow crushing gradients on the BOLD signal. In: Proceedings of the 2nd Annual Meeting of SMR, San Francisco, 1994.
19. Song AW, Woldorff M, Fichtenholtz H, Mangun GR, McCarthy G. Flow-sensitive alternating diffusion-weighting effect (FADE): vascular and parenchymal contributions to brain fMRI signal. In: Proceedings of the 9th Annual Meeting of ISMRM, Glasgow, Scotland, 2001.
20. Menon RS. Suppression of non-capillary BOLD signals through the use of phase fluctuations. In: Proceedings of the 9th Annual Meeting of ISMRM, Glasgow, Scotland, 2001.